Research article

Melt-casted Li$_{1.5}$Al$_{0.3}$Mg$_{0.1}$Ge$_{1.6}$(PO$_4$)$_3$ glass ceramic electrolytes: A comparative study on the effect of different oxide doping

Sofia Saffirio [a,b,c], Hamideh Darjazi [b,c], Marco Etzi Coller Pascuzzi [d],
Federico Smeacetto [a,*], Claudio Gerbaldi [b,c,**]

[a] GLANCE Group, Department of Applied Science and Technology (DISAT), Politecnico di Torino, C.so Duca degli Abruzzi 24, 10129, Torino, Italy
[b] GAME Lab, Department of Applied Science and Technology (DISAT), Politecnico di Torino, C.so Duca degli Abruzzi 24, 10129, Torino, Italy
[c] National Reference Center for Electrochemical Energy Storage (GISEL) - INSTM, Via G. Giusti 9, 50121, Firenze, Italy
[d] Fondazione Istituto Italiano di Tecnologia – IIT, CSFT@PoliTo, Via Livorno 60, 10144, Torino, Italy

ABSTRACT

The development of Li-ion conducting solid-state electrolytes (SSEs) is crucial to achieve increased energy density, operative reliability, and unprecedented safety to replace the state-of-the-art Li-ion battery (LIB). In this regard, we here present the successful melt-casting synthesis of a MgO-added NASICON-type LAGP glass-ceramic electrolyte with composition Li$_{1.5}$Al$_{0.3}$Mg$_{0.1}$Ge$_{1.6}$(PO$_4$)$_3$, namely LAMGP. The effects of three different additional oxides are investigated, with the aim to improve grain cohesion and consequently enhance Li-ion conductivity. Specifically, yttrium oxide (Y$_2$O$_3$, 5 mol%), boron oxide (B$_2$O$_3$, 0.7 mol%) and silicon oxide (SiO$_2$, 2.4 % mol) are added, yielding LAMGP-Y, LAMGP-B and LAMGP-Si, respectively. Their effects are exhaustively compared in terms of thermal, crystalline, structural/morphological and ion conducting features. Among the three oxides, B$_2$O$_3$ is able to positively act on grain boundaries without bringing along grains deformation and insulating secondary phases formation, achieving enhanced ionic conductivity of 0.21 mS cm^{-1} at 20 °C as compared to 0.08 mS cm^{-1} for a commercial LAGP subjected to the same thermal treatment. A remarkable anodic oxidation stability up to 4.8 V vs Li$^+$/Li is assessed by LAMGP-B system, which accounts for promising prospects for its use in combination with high-energy (high-V) cathodes.

1. Introduction

As a result of the worldwide efforts towards decarbonization, research on battery materials has gained prominence over the past decade amongst the main enabling technologies for the electrification of transportation and for the stationary storage of intermittently-produced renewable energy [1]. Despite having become the ubiquitous technology to power portable electronics, the market-leader Li-ion battery (LIB) cannot easily satisfy the requirements needed to address the large-sale market growth that is prospected over the next decades for electromobility (different power sources needed for different electric vehicles – EVs, *viz.*, high energy/power for top-class cars, durability and low cost for mini-EVs and city cars) and smart grid facilities (large-scale/volume battery needed) [2]. Due

---

* Corresponding author.
** Corresponding author. GAME Lab, Department of Applied Science and Technology (DISAT), Politecnico di Torino, C.so Duca degli Abruzzi 24, 10129, Torino, Italy.
E-mail addresses: federico.smeacetto@polito.it (F. Smeacetto), claudio.gerbaldi@polito.it (C. Gerbaldi).

to the use of a flammable liquid electrolyte solution for alkali metal (Li^+) ion transport, large-scale standard LIBs pose serious safety-related concerns; indeed, safety will become a major threat [3] for the full deployment of electrical energy storage (EES) technologies. Moreover, to achieve a widespread market penetration, high energy densities are required [4] to increase the endurance mileage of EVs, thus allowing to replace internal combustion engine (ICE) vehicles. In this regard, the use of solid-state lithium-based batteries (SSLBs) is a promising choice. Indeed, compared to commercial LIBs, a SSLB enables the use of cathodes having high-operating voltage combined with lithium metal anodes, achieving a 2/3-fold increase in energy density. Moreover, the use of a solid-state electrolyte (SSE), that simultaneously plays the role of ionic conductor and separator between the electrodes, enables both to save more internal space and increase the amount of active material, while also lightening the battery pack and addressing issues, such as decomposition at high anodic potentials, flammability and thermal runaways [5–8]. By using a SSE, improved chemical and electrochemical stability, along with mechanical robustness, are also addressed [9–12]. The proper combination of these features makes SSLBs very promising [13], and the need to develop advanced SSEs comes accordingly.

Among the most interesting inorganic solid electrolytes that are being explored in the past decades for energy storage applications are NASICON-type materials. Thanks to their relatively high ionic conductivities, in the range of 10^{-4}-10^{-3} S cm^{-1} at RT, almost at the level of liquid electrolytes, and thermal and mechanical stability [14], they possess great prospects in the development of SSLBs. Single Li-ion conducting NASICON-type compounds agree to the general formula Li $[M_2(PO_4)_3]$, where M are tetravalent cations, most commonly Ge, Ti or Zr. These compounds crystallize into a rhombohedral lattice where MO_6 octahedra share corners with PO_4 tetrahedra [15], giving rise to an ordered three-dimensional network that enables ion migration. Free Li^+ ions enter the solid solution upon substitution of trivalent (such as Al^{3+}) or bivalent (such as Mg^{2+}) cations for the tetravalent M cation, while maintaining the lattice symmetry. In this regard, it is important to point out that the ionic conductivity of these systems can be increased by either acting on the size of the conduction pathway or on the concentration or transport of mobile cations [16]. The first results from substituting M with cations having larger ionic radii, while the second increases with the decreasing valence number of the substituting cation, enabling an increased concentration of free lithium ions in the solution when charge neutrality is restored.

The Li_2O–Al_2O_3–GeO_2–P_2O_5 (LAGP) glass-forming system is a promising NASICON-structured glass-ceramic electrolyte used as a basis for producing electrolytes of the $Li_{1+x}Al_xGe_{2-x}$ $(PO_4)_3$ series [17]. These systems possess high thermal stability and good compatibility with 4 V-class electrode materials [18,19], and the $Li_{1.5}Al_{0.5}Ge_{1.5}(PO_4)_3$ composition is reported to have the highest ionic conductivity [20]. Over the past decades, the addition of different dopants in different concentrations in this family of electrolytes was investigated, mainly in terms of resulting ionic mobility [18,21–26]. The idea that, for a given number of free Li^+ ions available for conduction, Li^+ ion conductivity is not only dependent on the thermally-activated dynamics described by the Arrhenius law, but also on microstructural and morphological features, was already qualitatively postulated in previous studies [27–31], including our precedent work [32] on boron-oxide-added LAGTP. Nevertheless, no detailed evidence and demonstration of this were given before the study of Vyalikh et al. [33], who demonstrated that one of the most impactful factors behind this is grain cohesion. Through a deep NMR investigation on the mobility of Li^+ ions in NASICON-type glass-ceramic electrolytes, they demonstrated that structural modifications of the NASICON crystal lattice, upon addition of dopants, have a minor effect on lithium ion mobility. In terms of activation energies in fact, very similar E_a values were observed for systems showing different compositions (doped and undoped with Y_2O_3). However, a five-fold ionic conductivity enhancement could be observed in the sample showing an increased connectivity between the grains, highlighting the crucial role played by microstructure and morphology. Thus, having defined the concentration of mobile Li^+ ions on the basis of the system composition, the microstructural and morphological features play a crucial role in the development of highly conducting SSEs. In this regard, the presence of pores is also detrimental, due to the resulting reduction of active cross-section available for conduction [34]. Nevertheless, grain boundaries are even more impacting, being at a microstructural level throughout the entire polycrystalline material. The overall ionic conductivity of a ceramic/glass-ceramic electrolyte is in fact strongly reduced by the resistance exerted by grain boundaries [35], leading to an overall lowered conductivity in comparison with that of the bulk.

Given the conspicuous number of studies already available on the addition of different promising dopants to the LAGP system, as mentioned above, the purpose of the current work is not to propose striking new compositions with the aim to act on the crystal lattice of LAGP. Indeed, our focus here is rather to investigate the effect of the most promising types and concentrations of dopants reported in the recent literature, to evaluate the correlation between the resulting microstructural/morphological modifications and the related changes in ionic conductivity. To the authors' knowledge, a comparison among different dopants has not been reported from this perspective so far, and, actually, in our opinion it is highly important to drive the research toward the development of advanced, solid-state electrolyte separators made of NASICON-type glass-ceramics appealing for high-voltage SSLBs.

Specifically, according to the studies of Leo et al. [28] and Nikodimos et al. [29], a bare glass-ceramic $Li_{1.5}Al_{0.3}Mg_{0.1}Ge_{1.6}(PO_4)_3$ system, namely LAMGP, is here developed through a melt-casting technique, with a small modification in the Al content compared to the $Li_{1.6}Al_{0.4}Mg_{0.1}Ge_{1.5}(PO_4)_3$ system of reference (general formula $Li_{1+x+2y}Al_xMg_yGe_{2-x-y}$ $(PO_4)_3$), to avoid the formation of insulating $AlPO_4$, usually reported for values of $x \geq 0.3$ [15]. Being Mg^{2+} a divalent cation with a larger ionic radius of 66 p.m. compared to Ge^{4+} (53 p.m.), an increase in the size of channels for Li conduction is expected. Moreover, as a result of the substitution of divalent cations for tetravalent cations, the concentration of lithium ions being free for conduction is doubled. The addition to this LAMGP system of three different dopants acting on the cohesion of grain boundaries and/or on the shape of grains, i.e. on the microstructural and morphological features of the system, was investigated. In particular, diyttrium trioxide (Y_2O_3), diboron trioxide (B_2O_3) and silicon dioxide (SiO_2) were selected in the 5, 0.7, and 2.4 mol%, on the basis of the optimizations previously carried out by Vizgalov et al. [31], Jadhav et al. [36] and Das et al. [30], respectively. Considering the large ionic radius of Y^{3+} (90 p.m.) compared to Ge^{4+}, the addition of Y_2O_3 to the glass-ceramic does not result in the incorporation of Y into the crystalline LAGP solid solution, rather leading to the segregation of YPO_4 at the grain boundaries. B_2O_3 is instead an amorphous oxide that melts at ~450 °C inducing a reorganization

of grains and grain boundaries. Eventually, SiO_2 acts as a glass former in substitution for P_2O_5. The resulting glass-ceramic SSEs are thoroughly characterized and their properties and behaviour compared in terms of thermal, crystal phase, micro-structural/morphological and ion conductivity analyses, accompanied by an evaluation of the electrochemical stability for the most promising system.

2. Materials and methods

2.1. Synthesis of the NASICON-structured glass ceramics

The NASICON-structured glass ceramics were fabricated through a melt-casting technique. Precursors, including Li_2CO_3 (99.0 %, EMSURE ACS), Al_2O_3 (99.9 %, Alfa Aesar), $MgCO_3$ (99.99 %, Sigma-Aldrich), GeO_2 (99.99 %, Sigma-Aldrich), and $NH_4H_2PO_4$ (99.9 %, Carlo Erba), were utilized in stoichiometric proportions for the synthesis of the base material with a composition of $Li_{1.5}Al_{0.3}Mg_{0.1}Ge_{1.6}(PO_4)_3$, constituting $18.3Li_2O-3.7Al_2O_3-2.4MgO-39GeO_2-36.6P_2O_5$ (mol.%), referred to as LAMGP. Additionally, H_3BO_3 (99.5 %, Sigma-Aldrich), Y_2O_3 (99.99 %, Sigma-Aldrich), and SiO_2 (99 %, Honeywell) were individually introduced into LAMGP to form Y_2O_3-doped, B_2O_3-doped, and SiO_2-doped glass ceramics, denoted as LAMGP + 5 % mol Y_2O_3 (LAMGP-Y), LAMGP + 0.7 % mol B_2O_3 (LAGMP-B), and partially substituted $Li_{1.5}Al_{0.3}Mg_{0.1}Ge_{1.6}P_{2.9}Si_{0.1}O_{12}$ (LAMGP-Si, where Si accounts for 2.4 % mol of the overall molar composition), respectively. The molar contents of Y_2O_3 and B_2O_3, when rescaled to an overall 100 % molar composition, yield 4.76 and 0.69 % mol, respectively. For simplicity, throughout the current study, the approximated values of 5 and 0.7 % will be addressed. Precursors were thoroughly mixed for 24 h, transferred into an Al_2O_3 crucible, and placed in an electric furnace. a multi-step heating process was carried out to enable ammonia release at 350 °C, isothermal release of CO_2 at 700 °C, and final heating to 1350 °C for 1 h to achieve homogeneous melt formation. To account for and compensate specific lithium losses during melting at 1350 °C [37], 0.2 g of excess Li_2CO_3 (corresponding to 0.5 %wt) was added to each glass-ceramic system. The resulting glasses (LAMGP, LAMGP-B, LAMGP-Y, and LAMGP-Si) were cast onto a brass plate, and promptly transferred into a furnace at 470 °C for 2 h for stress relief. The annealed bulk glass then underwent a heat treatment at T_g+20 °C for 1 h to stimulate nucleation, followed by 12 h at 700 °C for grain growth. Both heating steps employed a heating rate of 5 °C min^{-1}. As a reference for ionic conductivity, commercial LAGP (Toshima Manufacturing Co., Ltd) underwent an identical heat treatment under comparable conditions.

2.2. Characterization techniques

The glass-ceramics characteristic temperatures, including glass transition (T_g), onset crystallization (T_x), and peak crystallization (T_p), were examined through differential thermal analysis (DTA, Netzsch, model DTA 404 PC) within the temperature range from 25 to 1100 °C (heating rate: 5 °C min^{-1}) under synthetic air conditions (N_2 + O_2 20 % ± 2 %). Heat treatments were defined accordingly, carrying out a nucleation step at T_g+20 °C followed by grain growth at 700 °C.

Crystalline phases were identified through X-ray diffraction analysis (XRD, Panalytical, Xpert3 MRD) performed at room temperature employing Cu Kα radiation, with a voltage of 40 kV and a current of 40 mA, in the 2θ range 10–70°. Refinement of these patterns via the Rietveld method was carried out by use of FullProf software, to estimate the actual lattice parameters and offering additional insights into the structural changes resulted from doping.

Scanning Electron Microscopy (SEM, Benchtop SEM, JCM-6000Plus, Jeol) was used to investigate the microstructural characteristics of each glass-ceramic material on fracture surfaces, exploiting secondary electrons (SEs) under high vacuum conditions and at a voltage of 5 kV. Elemental analysis was conducted through energy-dispersive X-ray spectroscopy (EDS, Jeol, EX-37001) at a voltage of 15 kV.

X-ray Photoelectron Spectroscopy (XPS) measurements were conducted on a PHI 5000 Versaprobe spectrometer equipped with a monochromatic Al Kα (1486.6 eV) X-ray source. An electron gun and an Ar ion gun were used to compensate for charging. The spot size was 100 µm and the pass energy was set at 187.85 and 23.5 eV for survey and high-resolution scans, respectively. Binding energy calibration was applied by setting the position of the C 1s sp^3 peak at 284.6 eV. The spectra were processed using CasaXPS software (v2.3.23, Casa Software Ltd).

For measurements of ionic conductivity, both sides of the polished samples underwent Pt sputtering. These Pt-coated electrolytes were then positioned between two ion-blocking stainless-steel (SS-316) electrodes and encased within an EL-Cell Std (EL-CELL, Germany) electrochemical test cell in SS/electrolyte/SS configuration. Evaluating ionic conductivity involved electrochemical impedance spectroscopy (EIS) conducted on a VMP3 potentiostat/galvanostat (Biologic, France) with a 20 mV oscillating potential within the frequency range from 300 kHz to 1 Hz. Testing occurred between −20 and 80 °C, utilizing an environmentally controlled climate chamber (MK 53 E2 from BINDER, Germany). Maintaining cells at each temperature for 2 h, with intervals of 10 °C, ensured 100 min of equilibration at each point. Nyquist plots were subject to analysis using Ec-Lab software (V 10.44). Ionic conductivity (σi) values were determined in accordance with equation (1):

$$\sigma_i = t/AR \qquad\qquad 1$$

where t is the thickness of the sample, A the area of the electrodes, and R the total resistance.

The Arrhenius plot (ionic conductivity *versus* the reciprocal of temperature $1/T$) was used to extract the activation energies (E_a) for the diffusion of Li$^+$ ion, according to equation 2:

$$\ln \sigma = \ln a - (E_a \, / \, RT) \qquad\qquad 2$$

being a the pre-exponential factor, and R the universal gas constant.

A fixed voltage (E) of 2 V was applied to a symmetric SS/electrolyte/SS cells with ion-blocking electrodes for 900 s at 25 °C, and the current response (I) was evaluated to obtain the DC resistance (R_{DC}) of the samples. The electronic conductivity (σ_e) was calculated as follows (equation (3)):

$$\sigma_e = t \, I \, / \, (A \, E) = t \, / \, (A \, R_{DC}) \qquad\qquad 3$$

The electrochemical stability window (ESW) of the most promising sample was investigated, according to the method developed and detailed in our previous study on LAGTP systems [32]. Overall, the cathodic stability window (CSW) was evaluated a three electrodes configuration in Swagelok-type T-cells assembled with lithium metal disks as both quasi reference (QRE) and counter (CE) electrodes, and glass-ceramic/conductive carbon composite as the working electrode (WE). The latter was prepared by mixing glass-ceramic powders (75 wt%), conductive carbon (C65, Imerys, 15 wt%) and polyvinylidene fluoride (PVDF) binder (Solef 6020, Solvay, 10 wt%) in NMP (N-methyl pyrrolidone, Merck) solvent, thus obtaining a viscous slurry, which is then coated on the current collector. Two Whatman GF/A glass fibre disks ($\approx$120 μm thick, 10 mm in diameter) were used as separator, soaked in a 1 M solution of lithium bis(trifluoromethanesulfonyl)imide (LiTFSI) in tetraethylene glycol dimethyl ether (G4, Solvionic, both battery grade) liquid electrolyte. Cyclic voltammetry (CV) tests were carried out on the VMP3 potentiostat/galvanostat at a scan rate of 0.1 mV s^{-1} in the range from 0.1 to 3 V vs. Li$^+$/Li at $\approx$ 25 °C. To determine the anodic stability window (ASW), a multi-layered cell was assembled constituted by a crosslinked (PEO-G4) polymer electrolyte [38,39] placed between Li metal and the LAGP-based systems, to avoid its reduction in contact with Li metal. To yield a two-electrode cell in the configuration Li/PEO-G4/ceramic/Au, an Au WE was sputtered onto the ceramic disk. The CV measurement was carried out in the range from 3 V up to 5.5 V vs. Li$^+$/Li at 0.1 mV s^{-1}.

3. Results and discussion

3.1. Thermal characterization

The thermal response of the LAMGP, LAMGP-Y, LAMGP-B and LAMGP-Si glass-ceramic systems was evaluated through DTA analysis (Fig. 1) to determine their characteristic temperatures.

The resulting values are listed in Table 1. Importantly, the two former parameters enabled us to determine the stability of a glass system, which is defined as the temperature difference between T_x and T_g with respect to T_g itself, i.e. $[T_x-T_g]/T_g$. The higher this value, the higher the stability of a glass and, thus, the lower its tendency to crystallize into a glass-ceramic system upon heating. On the other hand, T_p indicates the temperature value in correspondence of which the system reaches its maximum crystallization rate.

Regardless of the type of dopant (Y_2O_3, B_2O_3, SiO_2) and of the corresponding amount (5, 0.7, and 2.4 % mol, respectively) added to the bare LAMGP solid solution, the values of T_g of the doped systems under study showed an equal 10 °C increase compared to the LAMGP benchmark. Indeed, T_g indifferently increased from 480 to 490 °C upon the addition of Y_2O_3, B_2O_3, or SiO_2 to LAMGP, as reported in Table 1. On the contrary, the three dopants led to moderate differences in the values of T_x and T_p, which are indicators for the peculiar glass stability and crystallization response of each system. Specifically, the glass stability of the LAMGP system slightly increased upon the addition of 0.7 % mol B_2O_3 and 2.4 % mol SiO_2, and significantly increased upon the addition of 5 % mol Y_2O_3, according to the values listed in Table 1. This resulted in T_x values of 633, 627 and 670 °C, respectively, compared to 630 °C for undoped LAMGP. The marked stabilization in the presence of Y_2O_3 is likely ascribable to the consistently higher amount of dopant
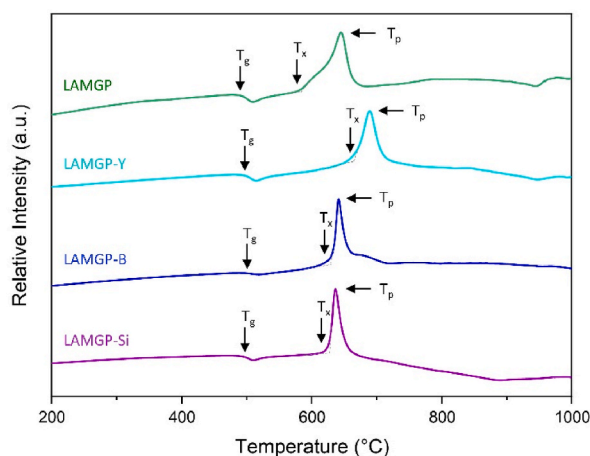

Fig. 1. DTA curves of as-casted LAMGP (green), LAMGP-Y (cyano), LAMGP-B (blue) and LAMGP-Si (violet) glass ceramics showing the characteristic thermal response of each system upon heating at 10 °C min^{-1}. The resulting characteristic temperatures are listed in Table 1 for comparison. (For interpretation of the references to colour in this figure legend, the reader is referred to the Web version of this article.)

Table 1

Comparison of the different onset glass-transition T_g, onset crystallization T_x and peak crystallization T_p temperatures detected through DTA analysis (Fig. 1) upon addition of Y_2O_3, B_2O_3 and SiO_2 (LAMGP-Y, LAMGP-B and LAMGP-Si, respectively) to the reference LAMGP glass-ceramic system, according to the compositions detailed in Paragraph 2.1.

System	T_g (°C)	T_x (°C)	T_p (°C)	$[T_g-T_x]/T_g$ (a.u.)
LAMGP	480	618	645	0.22
LAMGP-Y	490	670	690	0.37
LAMGP-B	490	633	641	0.29
LAMGP-Si	490	627	637	0.28

added in the solid solution (5 mol %), compared to B_2O_3 (0.7 mol%) and SiO_2 (2.4 mol%). The latter two resulted in fact in the same extent of stabilization, despite the % mol of B_2O_3 being down to nearly one fourth of that of SiO_2. When considering the peak crystallization temperature T_p instead, the addition of the three dopants resulted in a slight downward shift in the presence of B_2O_3 and SiO_2, and in a significant upward shift in the presence of Y_2O_3. Given the presence of a left shoulder broadening the peak of LAMGP, and thus increasing its crystallization temperature range, the addition of B_2O_3 and SiO_2 still led to increased glass stability compared to LAMGP, also as a combined result of their narrower crystallization peaks. Importantly, narrow peaks are representative for a faster crystallization [40].

It is noteworthy to emphasize that the systems under study are intended to be used as solid electrolytes in batteries. As a consequence, the stability of the as-cast glass up to high temperatures is not required for this type of application (standard temperature range of operation of −20 to 80 °C). It is rather more desirable to reduce its peak crystallization temperature, in order to achieve its full devitrification and to maximize its grain growth at a lower treatment temperature.

On the basis of the thermal responses discussed in this paragraph, LAMGP, LAMGP-Y, LAMGP-B and LAMGP-Si glasses were heat treated at 20 °C above T_g for 1 h to induce nucleation, and then at 700 °C for 12 h to achieve their devitrification, i.e. crystallization, and the consequent grain growth.

3.2. Crystalline phase analysis

XRD analysis was carried out on all of the glass ceramic systems under study to identify the crystalline phases formed upon their devitrification at 700 °C. The resulting diffractograms are shown in Fig. 2. The diffraction pattern of the main crystalline phase common to all systems is shown in the lower part of the figure, while reflections for the secondary phases are indexed in Fig. S2 (Supplementary Information) upon refinement of the patterns through the Rietveld method.

As expected, the conductive phase $LiGe_2(PO_4)_3$ (JCPDS reference code: 01-080-1924; major reflections at 25.159°, 21.307° and 21.477°) was identified as the main crystalline phase constituting all of the LAMGP-based glass-ceramic systems under study.

The presence of GeO_2 (JCPDS reference code: 01-083-2474; major reflections at 25.961°, 20.556° and 38.058°) insulating secondary phase was observed for each LAMGP-based composition, regardless of the type and content of added dopants. Additional diffraction peaks were detected in the LAMGP and LAMGP-Si samples corresponding to $AlPO_4$ (JCPDS reference code: 00-031-0028;
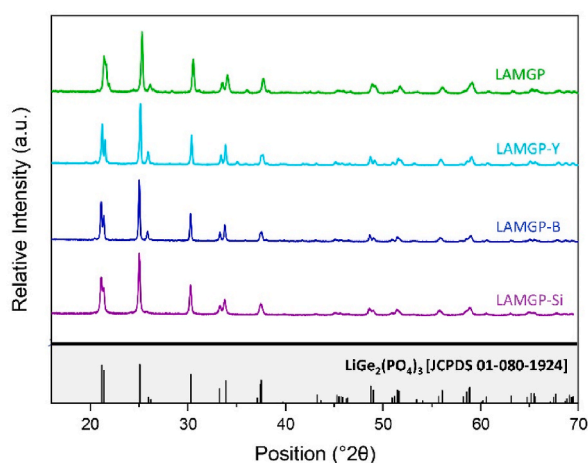

Fig. 2. XRD diffractograms recorded at ambient temperature for LAMGP (green), LAMGP-Y (cyano), LAMGP-B (blue) and LAMGP-Si (violet) glass-ceramic systems upon devitrification at 700 °C for 12 h. The pattern of the main conducting crystalline phase – $LiGe_2(PO_4)_3$ – constituting all samples is reported underneath (black) as a reference. Reflections of non-conducting secondary phases are instead indexed in Fig. S2 (Supplementary Information) highlighting the formation of different phases upon the addition of Y_2O_3, B_2O_3 or SiO_2. (For interpretation of the references to colour in this figure legend, the reader is referred to the Web version of this article.)

major reflections at 21.342°, 35.193° and 55.535°, the former easily overlapping with the second and third main peaks of $LiGe_2(PO_4)_3$ mentioned above), the most common secondary phase observed in LAGP and LATP systems along with GeO_2 [41–44]. The formation of $AlPO_4$ in both LAGP and LATP NASICON-type systems usually occurs as a result of the vaporization of lithium at increasing temperatures, and lithium loss has been registered at treatment temperatures above 900 °C [45,46]. In this regard, given the excess Li_2O added to each composition in view of the loss occurring during casting, and given the maximum treatment temperature of 700 °C reached for devitrification, $AlPO_4$ was not expected to form. The hypothesis for the presence of this secondary phase is therefore related to the possibility that also the treatment time, and not only the treatment temperature, has an impact on this phenomenon.

The addition of dopants to the LAMGP system did not lead to the formation of any further secondary phase, except for the LAMGP-Y system. B_2O_3 is in fact an amorphous oxide, melting at about 450 °C [36] and segregating at the grain boundaries, improving the cohesion among grains during the treatment. Thus, the absence of B-containing secondary phases is in good agreement with what is expected. No formation of secondary phases was either observed upon the addition of 2.4 mol% SiO_2 (LAMGP-Si, i.e. $Li_{1.5}Al_{0.3}Mg_{0.1}Ge_{1.6}P_{2.9}Si_{0.1}O_{12}$), in good agreement with the results shown by Das et al. [30], who reported the formation of secondary phases and a strong grain deformation for a higher SiO_2 content of 11.5 mol% ($Li_{1.5}Al_{0.3}Mg_{0.1}Ge_{1.6}P_{2.5}Si_{0.5}O_{12}$), which resulted in a significant drop in ionic conductivity. The appearance of an insulating phosphate (YPO_4, JCPDS reference code: 01-084-0335; major reflections at 25.873°, 35.035° and 51.806°) along with GeO_2 was instead observed in the presence of Y_2O_3.

To provide further insight into the structural change after doping, and to estimate the actual lattice parameters, the XRD patterns of the different LAMGP-based glass-ceramic systems under study were refined via the Rietveld method using the FullProf software (Fig. S2 in the Supplementary Information section) [47]. The lattice parameters of the LAMGP-based glass-ceramic systems under study are compared in Table 2. The cell parameters a and c, as well as the corresponding cell volume of the LAMGP, showed a slight enlargement compared to the standard data of LAGP [48], which is related to the bigger ionic radius of Mg^{2+} (66 p.m.) compared to Ge^{4+} (54 p.m.). Therefore, Mg^{2+} bivalent cations entered the LAGP crystalline structure substituting tetravalent Ge^{4+} cations, each substitution leading to the formation of two vacancies, *viz.* double the number of vacancies resulting from the substitution with Al^{3+} (49 p.m.). This suggested the effectiveness of the doping, which therefore resulted in doubled (in number) and larger vacancies for the conduction of Li^+ ions. Regarding the addition of further dopants to the LAMGP system, Y_2O_3 led to the a lattice contraction, while the c value was slightly increased. Given the ionic radius of Y^{3+} (90 p.m.) in comparison with Ge^{4+} (53 p.m.), Al^{3+} (49 p.m.) and Li^+ (76 p. m.), the introduction of Y_2O_3 in the glass was not expected to result in the incorporation of Y into the crystalline LAGP solid solution. Indeed, accordingly to Vizgalov et al. [31], yttrium segregates at the grain boundaries in the form YPO_4, in line with the results observed in this study. Peaks representative of this phosphate were in fact indexed in the XRD diffractogram as discussed above, and their clear evidence was presumably also due to the high content of Y_2O_3 (5 mol%). With the addition of B_2O_3 to the LAMGP system, the lattice constants a remained unchanged and c slightly increased, without leading to a significant overall distortion of the lattice. B_2O_3 is in fact not expected to enter the crystal lattice but rather to segregate at the grain boundary in the form of amorphous oxide, as clearly shown by Jadhav et al. [36] through TEM imaging. The use of SiO_2 dopant resulted instead in a contraction of both lattice constants and of the cell volume. This was mainly due to the doping with smaller Si^{4+} ions (41 p.m.) in place of Ge^{4+} (54 p.m.).

As compared to the reference diffraction pattern of $LiGe_2(PO_4)_3$, an overall shift (0.064°) of the diffraction peak positions was observed for all systems towards lower angles, in line with the changes in the lattice parameters of the main crystalline structure. This is ascribed to the doping of Si^{4+} atoms (41 p.m.) in place of P^{5+} (34 p.m.), and to that of Al^{3+} and Mg^{2+} in place of Ge^{4+} discussed above.

Summing up the XRD analysis results, Li^+ ion conducting $LiGe_2(PO_4)_3$ was identified as the main crystalline phase in all the LAMGP-based systems under study; the insulating secondary phase GeO_2 was observed in all samples, while the presence of $AlPO_4$ could be considered significant only in the LAMGP and LAMGP-Si samples. However, the SiO_2 was added without inducing the formation of any Si-containing secondary phase, while the addition of Y_2O_3 in LAMGP-Y led to the formation of insulating YPO_4. B_2O_3 was the only dopant not bringing along the formation of any secondary phases other than GeO_2, and for this reason considered the most promising system.

3.3. Microstructural characterization

The microstructural features of the developed glass-ceramic systems were investigated through Scanning Electron Microscopy (SEM) to evaluate the effect of different dopants on the grain cohesion and grain shape of the resulting single Li^+ ion conducting solid-state electrolytes. As discussed in the introduction, the microstructural and morphological features of crystalline ionic conductors are crucial for the overall Li^+ ion mobility.

The fracture surfaces of LAMGP, LAMGP-Y, LAMGP-B and LAMGP-Si were observed through SEs to investigate the effect of the three dopants on the morphologies of the resulting glass-ceramic electrolytes. Corresponding micrographs are shown in Fig. 3.

Table 2
Rietveld refinement results for LAMGP, LAMGP-Y, LAMGP-B and LAMGP-Si glass-ceramic electrolytes.

System	Lattice parameter (a and b/Å)	Lattice parameter (c/Å)	Cell volume (Å³)
LAMGP	8.276 (1)	20.619 (2)	1223.0
LAMGP-Y	8.267 (1)	20.671 (1)	1223.5
LAMGP-B	8.275 (1)	20.637 (1)	1224.0
LAMGP-Si	8.248 (2)	20.501 (1)	1207.9

The reference undoped LAMGP sample (Fig. 3a) was characterized by the formation of symmetric and homogeneous grains in terms of shape, with poor cohesion between the grains. The addition of Y_2O_3 to LAMGP induced the most noticeable changes in terms of grain morphology, resulting in squared and needle-like grains (Fig. 3b). This was accompanied by improved intergrain connectivity, ascribable to the segregation of cohesive YPO_4 at the grain boundaries, as discussed by Vyalikh et al. [33]. In this study, the formation of the phosphate is confirmed by the XRD results shown in paragraph 3.2. Such evident structural modifications are presumably also related to the high molar content of Y_2O_3 in the glass-ceramic composition. In this regard, a microstructural evaluation of the LAGP glass-ceramic system added with the same amount of Y_2O_3 was not reported by Vizgalov et al. [31].

A notable effect was observed also in the presence of B_2O_3. Indeed, despite its significantly lower molar concentration compared to Y_2O_3 (0.7 against 5 mol %, respectively), the addition of B_2O_3 resulted in remarkably continuous and cohesive grains (Fig. 3c). This is ascribable to the liquefaction of amorphous B_2O_3 occurring at around 450 °C [36] during the devitrification heat-treatment. However, unlike Y_2O_3, such an improvement was achieved without leading to any grain shape distortion. A deformation like the one induced by Y_2O_3 might in fact significantly drop the ionic conductivity of the system, especially in the presence of agglomerated needle-like grains [30], on the basis of the correlation reported by Vyalikh et al. [33] between grain morphology and cation mobility. The symmetric grain shape observed for LAMGP was instead fully preserved in the presence of B_2O_3. Besides, it is noteworthy to add that, being amorphous, B_2O_3 exclusively acts on the intergrain cohesion without inducing the formation of any insulating secondary phases, as observed in paragraph 3.2.

Eventually, according to Fig. 3d, the addition of SiO_2 did not have a noticeable impact on intergrain cohesion. On the contrary, it resulted in the formation of intragranular microcracks that would significantly inhibit ionic conduction. For the same SiO_2 content, this microcracking was not observed by Das et al. [30], who instead reported the deformation of grains into a needle-like shape responsible for ionic conductivity drop.

According to the SEM microstructural features discussed above, the addition of SiO_2 had a detrimental impact on the intergrain cohesion of LAMGP, which was instead significantly improved in the presence of Y_2O_3 and B_2O_3. However, only B_2O_3 was able to positively act on grain boundaries without bringing along the deformation of grains and the formation of insulating secondary phases, two factors that would negatively impact on the overall ionic conductivity of a glass-ceramic electrolyte.

3.4. Ionic conductivity and transport studies by EIS

In light of their use as separating electrolytes for truly solid-state Li-based batteries, the proposed Li-ion conducting glass-ceramic systems were tested for both their ionic conductivity at increasing temperatures and lithium ion transference number through electrochemical impedance spectroscopy (EIS).

The Nyquist plots resulting from the EIS analysis recorded at 20 °C in symmetric SS/electrolyte/SS cells for the LAMGP, LAMGP-Y, LAMGP-B and LAMGP-Si systems under study are shown in Fig. 4a, in comparison with commercial LAGP heat-treated under the same operating conditions. The corresponding ionic conductivity values in the temperature range between −20 and 80 °C are shown in the
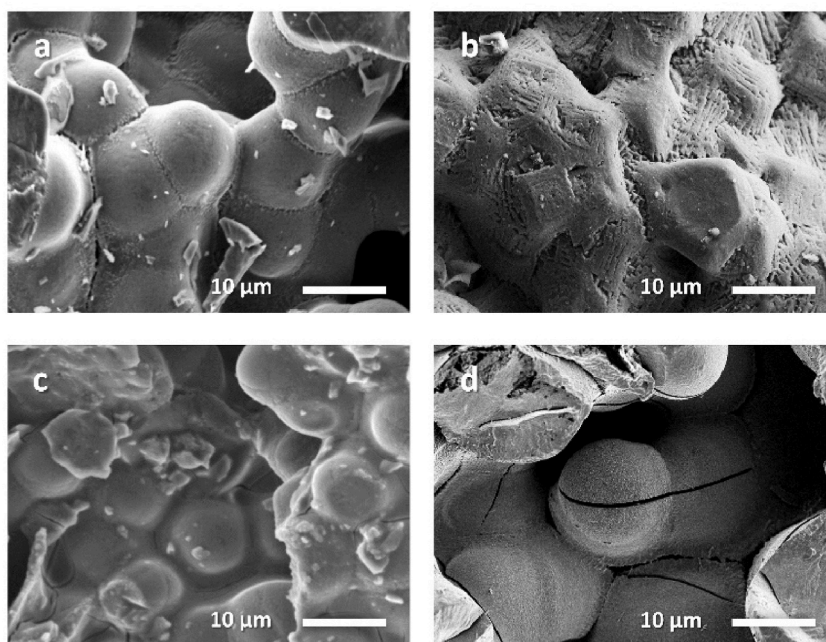

Fig. 3. SEM micrographs showing the morphological features of LAMGP (A), LAMGP-Y (B), LAMGP-B (C) and LAMGP-Si (D) glass ceramics. Secondary electrons (SEs) were used to analyse the fracture surfaces of the systems.

Arrhenius plot in Fig. 4b.

The EIS spectra of the most resistive samples (i.e., commercial LAGP, LAMGP and, particularly, LAMGP-Si) consist of a low-frequency straight line coupled with a high-frequency semicircle that does not intercept the origin. These spectra were fit using the upper equivalent circuit in the upper right corner of Fig. 4a. Constant phase elements (Q) were used to fit the straight lines with different inclinations at low frequencies and the slightly depressed semi-circles at high frequencies. As a result, in the equivalent circuit, straight lines are represented by Q2, corresponding to the capacitive contribution arising from the accumulation of charges at the ion-blocking electrode/electrolyte interface. The parallel combination of R2 and Q1 accounts instead for the high frequency semicircles (R2 and Q1 are attributed to the grain boundary resistance and capacitance, respectively). R1 represents the electrolyte bulk resistance, related to the distance of the high-frequency intercept with the real axis from the origin of the axes. The overall ionic resistance for commercial LAGP, LAMGP and LAMGP-Si was therefore evaluated as the sum of R1 and R2. In this respect, it is interesting to evidence how, by prolonging the high-frequency semi-circles, LAMGP would intercept the real axis at a slightly lower value (i.e., lower bulk resistance) than commercial LAGP, despite overlapping when considering the grain boundary contribution. This evidences the positive effect of MgO addition on the bulk (and not grain boundary) conduction of LAGP-based electrolytes. Indeed, as detailed in the introductory section, the substitution of Mg^{2+} (larger) for Ge^{4+} cations in the crystalline structure of LAGP results in wider channels for Li-ion conduction, contributing to lowering the bulk resistance. On the other hand, however, the grain boundary contribution to the overall resistance is increased in LAMGP-Si compared to LAMGP, suggesting a decreased grain-to-grain cohesion upon the addition of SiO_2, in good agreement with the microcracking observed and discussed in paragraph 3.3.

The resulting Arrhenius plots of ionic conductivity versus inverse temperature shown in Fig. 4b confirm this trend, reporting the lowest ionic conductivity value of 5.5×10^{-5} S cm^{-1} (~0.06 mS cm^{-1}) at 20 °C for LAMGP-Si, followed by 7.7×10^{-5} S cm^{-1} (~0.08 mS cm^{-1}) and 1.0×10^{-4} S cm^{-1} (~0.1 mS cm^{-1}) for commercial LAGP and LAMGP, respectively. The reader can refer to the overall transport properties extracted from the EIS analysis of the different glass ceramics under study, which are listed in Table 3. Also, kindly consider that the fitted resistance values at different temperature were obtained by applying eq. (1), carefully accounting for the area and thickness of the electrodes, which were slightly different for the different samples prepared in the form of pellets.

For the less resistive samples (i.e., LAMGP-Y and LAMGP-B), AC responses consist of an inclined straight line intercepting the real axis at non-zero high frequency values. Being the high-frequency semi-circle only hinted in this case, the spectra were fitted as the series combination of R3 (overall resistance) and Q2, according to the lower equivalent circuit reported in the top-right corner of Fig. 4a. Compared to SiO_2, the positive effect induced by the addition of Y_2O_3 or B_2O_3 to LAMGP was remarkable. The overall resistance of the systems was in fact nearly halved, resulting in ionic conductivity values of 1.8×10^{-4} S cm^{-1} (0.18 mS cm^{-1}) and 2.1×10^{-4} S cm^{-1} (0.21 mS cm^{-1}) at 20 °C in the presence of Y_2O_3 and B_2O_3, respectively. To our knowledge, these are amongst the highest ionic conductivity values reported so far [18,23,27–30] in the relevant literature for LAGP-based type of ceramic systems. Actually, an absolute comparison is usually not straightforward, considering that different instruments and instrumental setups are used to measure samples prepared in different laboratories, but still these ionic conductivity values are remarkable for LAGP-type ceramics, which normally show lower ionic conductivities than the parent LATP-based systems [14,24,32,34,35,46]. As mentioned in the previous paragraphs, B_2O_3 is an amorphous oxide that exclusively acts on grain cohesion and does not enter the LAGP solid solution. Similarly, Y_2O_3 does not enter the crystal lattice and it acts on grain cohesion through the segregation of YPO_4 at the grain boundaries. As a result, it can be concluded that the cohesive effect of Y_2O_3 has a major positive impact on ionic conductivity than the negative impact derived from being an isolating secondary phase. In this regard, Duluard et al. [49] reported that the presence of non-conductive secondary phases induces a densifying effect, which is beneficial for ionic conductivity, if their unit cell is smaller compared to that of the main conductive phase. Despite the comparable ionic conduction values for B_2O_3 and Y_2O_3, it is noteworthy to
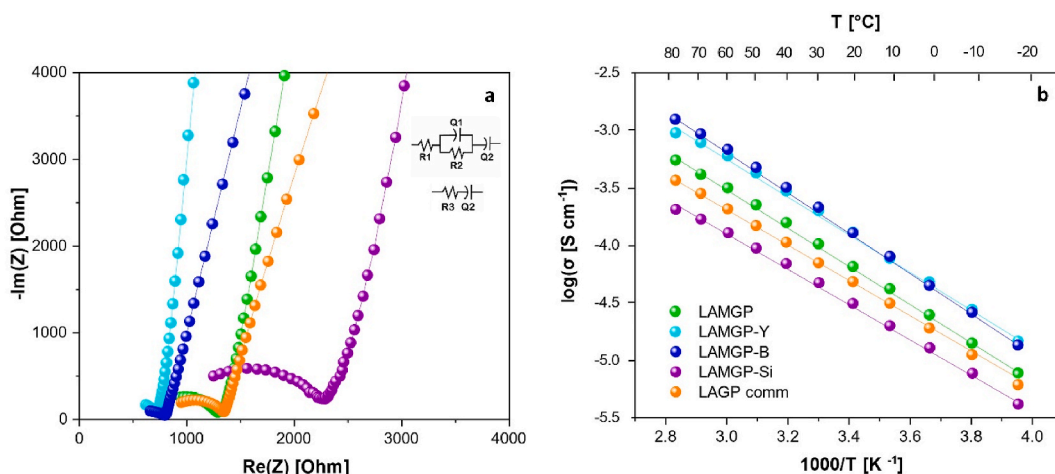

Fig. 4. (a) EIS Nyquist plots of symmetric SS/electrolyte/SS cells at 20 °C (equivalent circuits used to fit the spectra in inset); **(b)** Arrhenius plot of ionic conductivity data vs. 1000/T of the solid glass-ceramic electrolytes under study. The legend is representative for both the plots. Symbols stand for experimental data, straight lines for fitting curves.

Table 3
Summary of the transport properties extracted from the EIS analysis of LAMGP, LAMGP-Y, LAMGP-B and LAMGP-Si glass-ceramic electrolytes.

System	σ_e @ 25 °C [S cm^{-1}]	σ_i @ −10 °C [S cm^{-1}]	σ_i @ 20 °C [S cm^{-1}]	E_a [kJ mol^{-1}] (eV)	t_{Li+}
LAGP comm	5.2×10^{-10}	1.7×10^{-5}	7.7×10^{-5}	31.4 (0.33)	≥0.9999
LAMGP	4.8×10^{-10}	1.9×10^{-5}	1.0×10^{-4}	35.4 (0.37)	≥0.9999
LAMGP-Y	2.4×10^{-9}	4.1×10^{-5}	1.8×10^{-4}	32.5 (0.34)	≥0.9999
LAMGP-B	2.6×10^{-9}	3.8×10^{-5}	2.1×10^{-4}	33.0 (0.35)	≥0.9999
LAMGP-Si	3.0×10^{-10}	1.1×10^{-5}	5.5×10^{-5}	32.0 (0.33)	≥0.9999

underline that these improvements were obtained upon the addition of only 0.7 vs. 5 mol%, respectively. This brings to the straightforward conclusion that B_2O_3 is more effective than Y_2O_3 and, therefore, lower amounts (down to about 0.15 % compared to Y_2O_3) are sufficient to achieve a comparable improvement in terms of final ionic conductivity. Moreover, as previously discussed, B_2O_3 was able to positively affect grain cohesion without bringing along the deformation of grains and the formation of insulating secondary phases. Benefits can be addressed also in terms of impact and reliability, considering that both boron/borate and yttrium precursors were assessed as critical according to the latest EU critical-raw material (CRM) list (Fourth list of CRMs, *COM(2020) 474 - Critical Raw Materials Resilience: Charting a Path towards greater Security and Sustainability*), thus using lower amount is more sustainable.

The activation energies extrapolated from the Arrhenius plots are in the range of 0.33–0.39 eV (Table 3), in good agreement with those reported in the literature for similar systems [49–52] and also in line with the commercial LAGP tested as a reference in this study.

Eventually, in order to verify that the proposed Li-ion conducting glass-ceramic systems can act as a good separator between the positive and the negative electrodes in a SSLB, the electronic conductivity was evaluated through a DC method. Results shown in Fig. S2 (Supplementary Information) confirmed that the systems are pure ionic conductors, with ionic transference numbers ≥0.9999, as a result of negligible σ_e values in the order of 10^{-9}-10^{-10} S cm^{-1} at 25 °C (see Table 3).

Overall, LAMGP-B can be addressed as the most promising glass-ceramic system among those developed in the current study, resulting in grains with improved cohesion (Fig. 3, paragraph 3.3) with respect to LAMGP and, especially, LAMGP-Si. A comparable effect on grain cohesion is observed upon the addition of Y_2O_3. However, the higher amount of dopant required to achieve the same improvement in ionic conductivity brings along the formation of additional insulating secondary phases (Fig. 2, paragraph 3.2) and grain shape distortion (Fig. 3, paragraph 3.3). Moreover, as also discussed previously, the addition of increasingly higher amounts of CRMs is of course less convenient from a sustainable perspective. For these reasons, the most interesting result arising from the current study, also considering the sustainable development and up-scaling prospects, can be attributed to the use of B_2O_3, *viz.* LAMGP-B.

3.5. Electrochemical stability window (ESW) by cyclic voltammetry

For practical applications in batteries, it is fundamental to assess the stability of an electrolyte in the voltage window at which the electrodes operate inside the electrochemical cell.

The electrochemical stability of the most promising sample (i.e., LAMGP-B) was tested in the range of interest, separately cathodically and anodically, accordingly to the methods developed in our previous study [32] and detailed in paragraph 2.2. Based on this, LAMGP-B was used as the WE and evaluated by cyclic voltammetry (CV). Resulting profiles are shown in Fig. 5. In particular, when determining its cathodic stability window (CSW), the glass-ceramic material was milled and prepared in the form of composite electrodes containing C65 carbon as an electronic conducting additive, and then deposited on a Cu foil. Samples were housed in
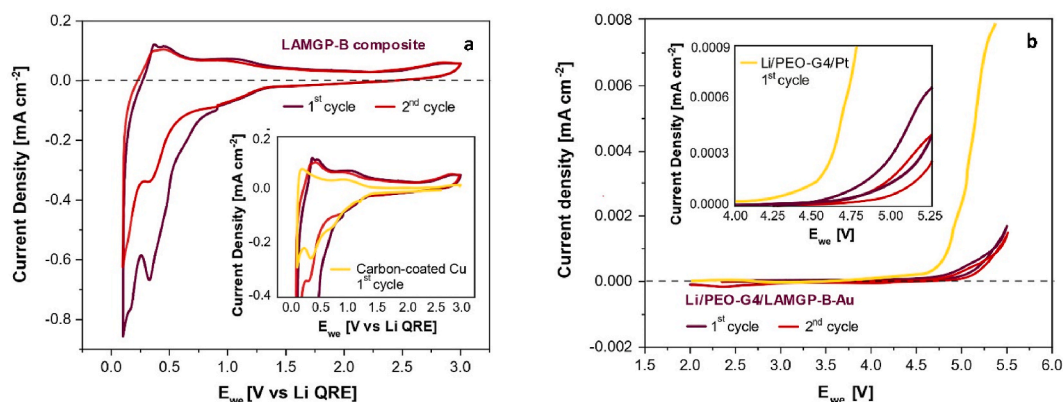

Fig. 5. CV scans at 0.1 mV s^{-1} and ≈25 °C of electrochemical cells cycled in cathodic/anodic potential ranges in the following configurations: **(a)** OCV – 0.1 V (CSW), in a three-electrode cell with Li metal CE and QRE, LiTFSI 1 M in G4 liquid electrolyte, and C-LAMGP-B composite (red line series) or CC-Cu (yellow line) WE; **(b)** OCV – 5.5 V (ASW), in a Li/PEO-G4/LAMGP-B/Au cell (red line series) and a Li/PEO-G4/Pt cell (one sweep, yellow line). (For interpretation of the references to colour in this figure legend, the reader is referred to the Web version of this article.)

Swagelok-type T-cells assembled in three-electrodes configurations, with Li metal disks as QRE and CE electrodes, and LiTFSI 1 M in G4 liquid electrolyte (Fig. 5a). On the other hand, a multi-layered cell containing a PEO-based polymer electrolyte (PEO-G4) as an interlayer between the Li metal electrode and the LAMGP-B ceramic was used to assess the anodic stability window (ASW) of the material (Fig. 5b), avoiding its reduction in contact with Li metal. The surface of the glass-ceramic sample was sputtered with Au to obtain a two electrodes cell in the configuration Li/PEO-G4/LAGTP-B-/Au.

CV scans of LAMGP-B composite WE in the range 3–0.1 V vs Li QRE are shown in Fig. 5a (red line, the bare CC-Cu profile is also reported in yellow for comparison). A small signal reduction below 1.4 V could be detected during the first cathodic sweep, indicating the reduction of LAGP [24]. At lower potentials, multiple peaks were observed. According to the literature, the peaks at 0.4 V [53] and 0.1 V [54] result from the formation of Li–Ge alloys, while those at approximately 0.5 and 0.3 V are related to the lithiation of Ge [55]. Reduction signals at 0.7 and 1 V are instead usually ascribed to the conversion of GeO_2 to $Ge + Li_2O$ [54]. The subsequent oxidation during the first sweep resulted in a peak at 0.4 V (Li dealloying) and in a broad signal with a maximum below 1.4 V (re-oxidation of Ge to GeO_2). The profiles and related reduction/oxidation peaks were rather maintained in the following cycles.

The conversion of GeO_2 to $Ge + Li_2O$, resulting from the $Ge^{4+} \rightarrow Ge^0$ reduction, was confirmed by XPS analysis. In this regard, Fig. S3 (Supplementary Information) shows the spectra of Ge 3d (Fig. S3a) and O 1s (Fig. S3b) for the LAMGP-B system before and after undergoing CV scans in the range 3–0.1 V vs Li QRE. The two samples are referred as *fresh* and *tested (*or *used)*, respectively. A clear peak located at ~32.6 eV was observed in the Ge 3d spectral region of the fresh sample and ascribed to Ge in its +4 oxidation state [56, 57]. This peak became negligible in intensity in the used sample and a new peak at ~29.3 eV appeared, corresponding to the presence of Ge^0 [54]. This result indicated that Ge was reduced during the electrochemical testing and converted to its metallic state. Considering the O 1s spectral region, instead, a peak at ~531 eV related to oxygen coming from phosphates [58] was detected in both samples, and an additional peak appeared at binding energies of ~527.8 eV in the spectrum of the tested sample, revealing the formation of Li_2O [58] and thus confirming the conversion of GeO_2 to $Ge + Li_2O$ in the sample after electrochemical testing.

To assess the ASW of LAMGP-B, CV measurements were carried out at 0.1 mV s^{-1} up to 5.5 V (Fig. 5b). Under this condition, a negligible oxidation current started flowing at approximately 4.50 V, followed by an exponential increase with onset voltage of oxidative degradation at $\approx$ 4.80 V. The resulting oxidation stability of the highly conductive LAMGP system under study is sufficiently high to account for safe operation with high energy density 4 V-class cathodes (e.g., NMC series of materials, LNMO or Li-rich layered oxides), while, cathodically, the operational voltage should be carefully controlled and limited to prevent Ge^{4+} reduction below 1.5 V vs Li, and the direct contact with the lithium metal electrode avoided (or Li metal protected) to prevent its progressive degradation upon cycling.

4. Conclusions

In the present work, we investigated the effect of the most promising types and concentrations of dopants reported in the recent literature to evaluate the correlation between the resulting microstructural/morphological modifications and the related changes in ionic conductivity. As a result, we have reported the successful preparation of a glass-ceramic LAMGP system with the chemical formula $Li_{1.5}Al_{0.3}Mg_{0.1}Ge_{1.6}(PO_4)_3$, using a melt-casting technique, and the thorough investigation in terms of the resulting crystalline phases, microstructures and ionic conductivities after the addition of different oxides, *viz.* Y_2O_3, B_2O_3 and SiO_2. The main conductive crystalline phase $LiGe_2(PO_4)_3$ was identified in all the LAMGP-based systems under study, along with the insulating secondary phase GeO_2. $AlPO_4$ was also observed in the LAMGP system, and upon the addition of SiO_2. B_2O_3 was successfully added without inducing the formation of any further secondary phase other than GeO_2, while Y_2O_3 led to the formation of an insulating YPO_4 phase. However, this phosphate, known for segregating at the grain boundaries, enabled to achieve improved intergrain cohesion and a corresponding ionic conductivity value of 0.18 mS cm^{-1} at 20 °C, higher than the 0.08 mS cm^{-1} registered for commercial LAGP at the same temperature. A slightly higher ionic conductivity value of 0.21 mS cm^{-1} at 20 °C was observed while adding B_2O_3, which is actually remarkable if we consider that this improvement was obtained upon the addition of only 0.7 mol% B_2O_3 vs 5 mol% Y_2O_3. Moreover, unlike Y_2O_3, B_2O_3 was able to positively act on grain boundaries without bringing along the deformation of grains and the formation of insulating secondary phases. On the other hand, the addition of SiO_2 had a detrimental impact on the intergrain cohesion of LAMGP, leading to significant microcracking of the system. This, along with the presence of secondary phases, explains the increased resistive contribution in EIS.

Overall, based on our findings, the LAMGP-B glass-ceramic can be addressed as the most promising system among those investigated in the current study, with improved grain cohesion and preserved grain shape, absence of further insulating secondary phases other than GeO_2 and a remarkable anodic oxidation stability up to 4.8 V vs Li$^+$/Li, enabling its use in Li-based batteries in combination with high energy density 4 V-class cathodes. As discussed in the text, based on the EU regulations and CRM survey map, the selection of B_2O_3, which induces positive changes even when added at very low amounts compared to Y_2O_3, is also impactful in terms of more sustainable production of solid-state battery electrolytes. Of course, optimization has to be foreseen particularly in enhancing the cathodic stability, in combination with proper interface engineering/protection for avoiding direct contact with the lithium metal electrode, thus allowing the practical use in SSLBs, which is the aim of our ongoing research activity.

Data availability

The raw/processed data required to reproduce these findings cannot be shared at this time due to technical or time limitations.

CRediT authorship contribution statement

Sofia Saffirio: Writing - review & editing, Writing - original draft, Visualization, Validation, Methodology, Investigation, Formal analysis, Data curation. **Hamideh Darjazi:** Writing - original draft, Validation, Investigation, Formal analysis, Data curation. **Marco Etzi Coller Pascuzzi:** Investigation, Formal analysis. **Federico Smeacetto:** Writing - review & editing, Supervision, Resources, Funding acquisition, Conceptualization. **Claudio Gerbaldi:** Writing - review & editing, Supervision, Resources, Funding acquisition, Conceptualization.

Declaration of competing interest

The authors declare that they have no known competing financial interests or personal relationships that could have appeared to influence the work reported in this paper.

Acknowledgement

Appendix A. Supplementary data

Supplementary data to this article can be found online at https://doi.org/10.1016/j.heliyon.2024.e24493.

References

[1] H. Rahimi-Eichi, et al., Battery management system: an overview of its application in the smart grid and electric vehicles, IEEE Ind. Electron. Mag. 7 (2) (2013) 4–16.

[2] T. Famprikis, et al., Fundamentals of inorganic solid-state electrolytes for batteries, Nat. Mater. 18 (12) (2019) 1278–1291, https://doi.org/10.1038/s41563-019-0431-3.

[3] Q. Zhao, et al., Designing solid-state electrolytes for safe, energy-dense batteries, Nat. Rev. Mater. 5 (3) (2020) 229–252, https://doi.org/10.1038/s41578-019-0165-5.

[4] X. Yang, et al., Recent advances and perspectives on thin electrolytes for high-energy-density solid-state lithium batteries, Energy Environ. Sci. 14 (2) (2021) 643–671.

[5] G. Cui, Reasonable design of high-energy-density solid-state lithium-metal batteries, Matter 2 (4) (2020) 805–815, https://doi.org/10.1016/j.matt.2020.02.003.

[6] Z. Gao, et al., Promises, challenges, and recent progress of inorganic solid-state electrolytes for all-solid-state lithium batteries, Adv. Mater. 30 (17) (2018) 1–27, https://doi.org/10.1002/adma.201705702.

[7] Y.K. Sun, Promising all-solid-state batteries for future electric vehicles, ACS Energy Lett. 5 (10) (2020) 3221–3223, https://doi.org/10.1021/acsenergylett.0c01977.

[8] F. Hao, et al., Architectural design and fabrication approaches for solid-state batteries, MRS Bull. 43 (10) (2018) 746–751, https://doi.org/10.1557/mrs.2018.211.

[9] J.A. Lewis, et al., Chemo-mechanical challenges in solid-state batteries, Trends in Chemistry 1 (9) (2019) 845–857.

[10] K. Takada, Progress and prospective of solid-state lithium batteries, Acta Mater. 61 (3) (2013) 759–770.

[11] D.W. McOwen, et al., 3D-Printing electrolytes for solid-state batteries, Adv. Mater. 30 (18) (2018) 1–7, https://doi.org/10.1002/adma.201707132.

[12] C. Wang, et al., Garnet-type solid-state electrolytes: materials, interfaces, and batteries, Chem. Rev. 120 (10) (2020) 4257–4300.

[13] O. Sheng, et al., A decade of progress on solid-state electrolytes for secondary batteries: advances and contributions, Adv. Funct. Mater. 31 (27) (2021) 2100891.

[14] M. Hou, et al., Challenges and perspectives of NASICON-type solid electrolytes for all-solid-state lithium batteries, Nanotechnology 31 (13) (2020) 132003.

[15] M. Weiss, et al., Correlating transport and structural properties in $Li_{1+x}Al_xGe_{2-x}(PO_4)_3$ (LAGP) prepared from aqueous solution, ACS Appl. Mater. Interfaces 10 (12) (2018) 10935–10944.

[16] J.C. Bachman, et al., Inorganic solid-state electrolytes for lithium batteries: mechanisms and properties governing ion conduction, Chem. Rev. 116 (1) (2016) 140–162.

[17] S.V. Pershina, et al., Solid electrolyte membranes based on $Li_2O–Al_2O_3–GeO_2–SiO_2–P_2O_5$ glasses for all-solid state batteries, Membranes 12 (no. 12) (2022), https://doi.org/10.3390/membranes12121245.

[18] H. Kun, et al., Influence of Al_2O_3 additions on crystallization mechanism and conductivity of $Li_2O–Ge_2O–P_2O_5$ glass–ceramics, Phys. B Condens. Matter 406 (20) (2011) 3947–3950.

[19] S. V Pershina, et al., Effect of $Li_2O–Al_2O_3–GeO_2–P_2O_5$ glass crystallization on stability versus molten lithium, J. Non-Cryst. Solids 527 (2020) 119708.

[20] Y. Meesala, et al., Recent advancements in Li-ion conductors for all-solid-state Li-ion batteries, ACS Energy Lett. 2 (12) (2017) 2734–2751.

[21] L. Liu, et al., Improved ion conductivity and interface characteristics of the Te-doped solid nasicon electrolyte Li1. 5Al0. 5Ge1. 5 (PO4) 3 with graphite coating, J. Power Sources 575 (2023) 233137.

[22] R. Chen, et al., The pursuit of solid-state electrolytes for lithium batteries: from comprehensive insight to emerging horizons, Mater. Horiz. 3 (6) (2016) 487–516.

[23] Y.C. Kim, et al., Improving the ionic conductivity of $Li_{1+x}Al_xGe_{2-x}(PO_4)_3$ solid electrolyte for all-solid-state batteries using microstructural modifiers, Ceram. Int. 46 (14) (2020) 23200–23207, https://doi.org/10.1016/j.ceramint.2020.06.101.

[24] D.H. Kothari, et al., Effect of doping of trivalent cations Ga^{3+}, Sc^{3+}, Y^{3+} in $Li_{1.3}Al_{0.3}Ti_{1.7}(PO_4)_3$ (LATP) system on Li+ ion conductivity, Phys. B Condens. Matter 501 (2016) 90–94, https://doi.org/10.1016/j.physb.2016.08.020.

[25] P. Goharian, et al., Lithium ion-conducting glass-ceramics in the system Li$_2$O-TiO$_2$-P$_2$O$_5$-Cr$_2$O$_3$-SiO$_2$, J. Non-Cryst. Solids 409 (2015) 120–125, https://doi.org/10.1016/j.jnoncrysol.2014.11.016.
[26] J. Yang, et al., Titanium dioxide doping toward high-lithium-ion-conducting Li1.5Al0.5Ge1.5(PO4)3 glass-ceramics for all-solid-state lithium batteries, ACS Appl. Energy Mater. 2 (2019) 7299–7305.
[27] A. Curcio, et al., Ultrafast crystallization and sintering of Li$_{1.5}$Al$_{0.5}$Ge$_{1.5}$(PO$_4$)$_3$ glass and its impact on ion conduction, ACS Appl. Energy Mater. 5 (11) (2022) 14466–14475.
[28] C.J. Leo, et al., Effect of MgO addition on the ionic conductivity of LiGe$_2$(PO$_4$)$_3$ ceramics, Solid State Ionics 159 (3–4) (2003) 357–367, https://doi.org/10.1016/S0167-2738(03)00032-8.
[29] Y. Nikodimos, et al., A new high-Li$^+$-conductivity Mg-doped Li$_{1.5}$Al$_{0.5}$Ge$_{1.5}$(PO$_4$)$_3$ solid electrolyte with enhanced electrochemical performance for solid-state lithium metal batteries, J. Mater. Chem. A 8 (48) (2020) 26055–26065, https://doi.org/10.1039/d0ta07807g.
[30] A. Das, et al., Study on electrical and structural properties in SiO$_2$ substituted Li$_2$O-Al$_2$O$_3$-GeO$_2$-P$_2$O$_5$ glass-ceramic systems, Ceram. Int. 44 (11) (2018) 13373–13380, https://doi.org/10.1016/j.ceramint.2018.04.172.
[31] V.A. Vizgalov, et al., Enhancing lithium-ion conductivity in NASICON glass-ceramics by adding yttria, CrystEngComm 20 (10) (2018) 1375–1382, https://doi.org/10.1039/c7ce01910f.
[32] S. Saffirio, et al., Li$_{1.4}$Al$_{0.4}$Ge$_{0.4}$Ti$_{1.4}$(PO$_4$)$_3$ promising NASICON-structured glass-ceramic electrolyte for all-solid-state Li-based batteries: unravelling the effect of diboron trioxide, J. Eur. Ceram. Soc. 42 (3) (2022) 1023–1032.
[33] A. Vyalikh, et al., NMR studies of Li mobility in NASICON-type glass-ceramic ionic conductors with optimized microstructure, J. Mater. Chem. A 7 (23) (2019) 13968–13977, https://doi.org/10.1039/c8ta11686e.
[34] A. Rossbach, et al., Structural and transport properties of lithium-conducting NASICON materials, J. Power Sources 391 (March) (2018) 1–9, https://doi.org/10.1016/j.jpowsour.2018.04.059.
[35] A. Mertens, et al., Superionic bulk conductivity in Li$_{1.3}$Al$_{0.3}$Ti$_{1.7}$(PO$_4$)$_3$ solid electrolyte, Solid State Ionics 309 (2017) 180–186.
[36] H.S. Jadhav, et al., Influence of B$_2$O$_3$ addition on the ionic conductivity of Li1.5Al0.5Ge0.5(PO4)3 glass ceramics, J. Power Sources 241 (2013) 502–508, https://doi.org/10.1016/j.jpowsour.2013.04.137.
[37] L. Brewer, et al., The vapor pressures of lithium and sodium oxides, J. Phys. Chem. 59 (5) (1955) 421–425.
[38] C. Gerbaldi, et al., UV-curable siloxane-acrylate gel-copolymer electrolytes for lithium-based battery applications, Electrochim. Acta 55 (2010) 1460–1467.
[39] M. Falco, et al., Understanding the effect of UV-induced cross-linking on the physicochemical properties of highly performing PEO/LiTFSI-Based polymer electrolytes, Langmuir 35 (2019) 8210–8219.
[40] M. Li, et al., Study on crystallization process of Li$_2$O–Al$_2$O$_3$–SiO$_2$ glass-ceramics based on in situ analysis, Materials 15 (22) (2022) 8006.
[41] S. V Pershina, et al., Glass-ceramics in Li1+ xAlxGe2-x (PO4) 3 system: the effect of Al2O3 addition on microstructure, structure and electrical properties, J. Alloys Compd. 835 (2020) 155281.
[42] L. He, et al., Solid-state electrolytes: advances and perspectives, Funct. Mater. Lett. 14 (3) (2021) 2130001.
[43] J.S. Thokchom, et al., The effects of crystallization parameters on the ionic conductivity of a lithium aluminum germanium phosphate glass–ceramic," J. Power Sources 195 (9) (2010) 2870–2876.
[44] S. Cretu, et al., The Impact of Inter-grain Phases on the Ionic Conductivity of LAGP Solid Electrolyte Prepared by Spark Plasma Sintering, 2022 *arXiv Prepr. arXiv2211.06129*.
[45] E. Antolini, Lithium loss from lithium cobalt oxide: hexagonal Li Co O to 0.5 0.5 cubic Li$_{0.065}$Co$_{0.935}$O phase transition, Int. J. Inorg. Mater. 3 (2001) 721–726.
[46] K. Waetzig, et al., An explanation of the microcrack formation in Li$_{1.3}$Al$_{0.3}$Ti$_{1.7}$(PO$_4$)$_3$ ceramics, J. Eur. Ceram. Soc. 36 (8) (2016) 1995–2001, https://doi.org/10.1016/j.jeurceramsoc.2016.02.042.
[47] J. Rodriguez-Carvajal, Recent advances in magnetic structure determination by neutron powder diffraction, Phys. B Condens. Matter 192 (1–2) (1993) 55–69.
[48] S.V. Pershina, E.G. Vovkotrub, B.D. Antonov, Effects of B$_2$O$_3$ on crystallization kinetics, microstructure and properties of Li$_{1.5}$Al$_{0.5}$Ge$_{1.5}$(PO$_4$)$_3$-based glass-ceramics, Solid State Ion 383 (2022) 115990.
[49] S. Duluard, et al., Dense on porous solid LATP electrolyte system: preparation and conductivity measurement, J. Am. Ceram. Soc. 100 (1) (2017) 141–149.
[50] J.S. Thokchom, et al., Composite effect in superionically conducting lithium aluminium germanium phosphate based glass-ceramic, J. Power Sources 185 (1) (2008) 480–485.
[51] J.S. Thokchom, et al., Superionic conductivity in a lithium aluminum germanium phosphate glass–ceramic, J. Electrochem. Soc. 155 (12) (2008) A915.
[52] K. Hayamizu, et al., Long-range Li ion diffusion in NASICON-type Li$_{1.5}$Al$_{0.5}$Ge$_{1.5}$ (PO$_4$)$_3$ (LAGP) studied by 7 Li pulsed-gradient spin-echo NMR, Phys. Chem. Chem. Phys. 19 (34) (2017) 23483–23491.
[53] J.S. Peña, et al., Electrochemical reaction between lithium and β-quartz GeO$_2$, Electrochem. Solid State Lett. 7 (9) (2004) A278.
[54] W.G. Hwang, et al., State-selected photodissociation dynamics of CS$_2^+$ in the C$_2$Σ$_g^+$ state, J. Chem. Phys. 113 (2000) 4153–4157.
[55] G.-T. Kim, et al., Behavior of germanium and silicon nanowire anodes with ionic liquid electrolytes, ACS Nano 11 (6) (2017) 5933–5943.
[56] S. Kim, et al., Formation characteristics and photoluminescence of Ge nanocrystals in HfO$_2$, J. Appl. Phys. 105 (2009) 106112.
[57] Y. Qipeng, et al., Constructing Effective Interfaces for Li$_{1.5}$Al$_{0.5}$Ge$_{1.5}$(PO$_4$)$_3$ Pellets to achieve room-temperature hybrid solid-state Lithium metal batteries, ACS Appl. Mater. Interfaces 11 (10) (2019) 9911–9918.
[58] S. Wang, et al., Interfacial chemistry in solid-state batteries: formation of interphase and its consequences, J. Am. Chem. Soc. 140 (2018) 250–257.